RSC Advances

PAPER

View Article Online
View Journal | View Issue

Cite this: *RSC Adv.*, 2017, 7, 6093

# Site-selective Eu(III) spectroscopy of highly efficient luminescent mixed-metal Pb(II)/Eu(III) coordination polymers†

C. D. E. S. Barbosa,[ab] L. L. da Luz,[a] F. A. Almeida Paz,[c] O. L. Malta,[a] M. O. Rodrigues,[d] S. A. Júnior,[a] R. A. S. Ferreira[b] and L. D. Carlos*[b]

Received 6th December 2016
Accepted 9th January 2017

DOI: 10.1039/c6ra27850g

www.rsc.org/advances

Novel mixed-metal coordination polymers (CPs) based on $Pb_{1-x}Eu_x$–BDC ($x = 0.05$, 0.10, 0.25, 0.50 and BDC = 1,4-benzenedicarboxylic acid) are reported. The materials display different coordination structures as the Pb : Eu metal ratio is modified. Whereas for $x < 0.25$ the $Eu^{3+}$ ions essentially replace the $Pb^{2+}$ ones in the $[Pb(BDC)_n]$ structure, for $x > 0.25$ the samples are isotypical with $[Eu_2(BDC)_3(H_2O)_4]$, as shown by powder (including Rietveld analysis) and single-crystal X-ray diffraction. The unique $Pb_{0.75}Eu_{0.25}$–BDC compound displays a mixture of both crystalline phases with the highest emission quantum yield value reported for luminescent CPs based on Pb(II), 69 ± 7%. Site-selective excitation using a common Xe lamp permits the detailed study of the two $Eu^{3+}$ local sites, illustrating how powerful the $Eu^{3+}$ luminescence is as a local probe spectroscopic tool.

## Introduction

Coordination polymers (CPs) and Metal–Organic Frameworks (MOFs) constitute ionic classes of hybrid materials having received a wide scientific attention.[1–4] The hybrid character of these materials arising from the coordination between metal ions (or their clusters) and multifunctional organic ligands grant them a wide range of applications.[4–6] Mixed-ligand and mixed-metal CPs have been then synthesized through distinct synthetic protocols based in mixtures of different types of organic ligands and metal ions.[7–10] The presence of more than one metal ion or organic ligand in CP structures permits a fine tuning of the material's properties, *e.g.*, optical, catalytic, electronic, host–guest, magnetic, shape specificity and ion exchange.[11–15]

In particular, Pb-containing CPs present interesting luminescent properties,[16–18] and mixed-metal materials based on $Pb^{2+}$ have been previously reported.[19–21] Nevertheless, materials based on $Pb^{2+}$ and $Ln^{3+}$ ions are scarce. The first example of a 6p–4f heterometallic MOF was reported by Wang *et al.*[22] and, more recently, Pan *et al.* showed white-light emission in two series of heteronuclear $Pb^{2+}$–$Ln^{3+}$ complexes.[23]

Here, we report new photoluminescent 6p–4f heterometallic CPs, based on distinct $Pb^{2+}/Eu^{3+}$ ratios and 1,4-benzenedicarboxylic acid (BDC). The $Pb_{1-x}Eu_x$–BDC ($x = 0.05$, 0.10, 0.25, 0.50 and 1.00) materials were characterized by X-ray powder diffraction, single crystal X-ray diffraction and luminescence spectroscopy. Whereas for $x = 0.05$ and 0.10 the $Pb_{1-x}Eu_x$–BDC compounds are structurally similar to $[Pb(BDC)]_n$,[24–27] for $x = 0.50$ the CP exhibits the structure of the $[Eu_2(BDC)_3(H_2O)_4]$ hydrated phase.[28,29] The $Pb_{0.75}Eu_{0.25}$–BDC compound displays a mixture of both crystalline phases with a intriguing high emission quantum yield (69 ± 7%). Moreover, site-selective and time-resolved spectroscopy enabled the detailed study of the two $Eu^{3+}$ local sites in that CP illustrating how powerful the $Eu^{3+}$ luminescence is as a local probe spectroscopic tool. Although $Eu^{3+}$ luminescence was often used as a local structural probe in nanoparticles,[30,31] sol–gel derived hybrid materials[32,33] and ceramics,[34,35] this is, as far as we know, the first example of the use of this powerful tool in CPs and MOFs.

## Experimental

### Synthesis

Disodium terephthalate, $C_6H_4(COONa)_2$ ($Na_2BDC$, lç 0 Alfa Aesar, 99.0%), $Pb(NO_3)_2$ (VETEC, 99.0%) and $Eu(NO_3)_3 \cdot 5H_2O$ (Aldrich, 99.9%) were analytical grade and used as purchased. All solutions were prepared with ultrapure water. With the overall aim to include in the $Pb^{2+}$–terephthalic acid optically-active as $Eu^{3+}$ ions in order to design new photoluminescent

---

[a] *University Federal of Pernambuco, Department of Chemistry, Laboratório de Terras Raras, 50590-470, Recife, Brazil*

[b] *Department of Physics and CICECO – Aveiro Institute of Materials, University of Aveiro, 3810-193 Aveiro, Portugal. E-mail: lcarlos@ua.pt*

[c] *Department of Chemistry, CICECO – Aveiro Institute of Materials, University of Aveiro, 3810-193 Aveiro, Portugal*

[d] *University of Brasília (IQ – UNB), Campus Universitário Darcy Ribeiro, LIMA – Laboratório de Inorgânica e Materiais, 70904970, Brasília, Brazil*

† Electronic supplementary information (ESI) available: Crystallographic data, excitation spectrum and lifetime decay curves. CCDC 1490068. For ESI and crystallographic data in CIF or other electronic format see DOI: 10.1039/c6ra27850g

materials, $Pb_{1-x}Eu_x$–BDC ($x = 0.05, 0.10, 0.25, 0.50$) CPs were prepared using different $Pb^{2+}/Eu^{3+}$ (mmol mmol$^{-1}$) molar ratios (0.95 : 0.05, 0.90 : 0.10, 0.75 : 0.25, 0.50 : 0.50) and 0.50 mmol of $Na_2BDC$, with 14 mL of $H_2O$. The mixture was transferred to Teflon® lined autoclaves (25 mL) and the reaction took place under static hydrothermal conditions in ovens preheated at 393 K over a period of 3 days. The obtained materials were filtered, washed at room temperature with ultrapure water and dried at 313 K. For comparative purposes, the monometallic $[Pb(BDC)]_n$ and $[Eu_2(BDC)_3(H_2O)_4]$ CPs were synthesized following the same procedure described above.

### Scanning electron microscopy (SEM)

SEM images of $Pb_{1-x}Eu_x$–BDC ($x = 0.05, 0.10, 0.25$ and $0.50$) were acquired using a Shimadzu SS550 microscope with a tungsten filament operated at 15–20 kV. SEM images of the $[Pb(BDC)]_n$ and $[Eu_2(BDC)_3(H_2O)_4]$ CPs were collected using a Hitachi TM3000 microscope operated at 20 kV.

### Powder X-ray diffraction (PXRD)

The PXRD data were collected at room temperature (300 K) on a Bruker D8 Advance powder X-ray diffractometer using Bragg–Brentano geometry with Cu $K_\alpha$ radiation. The diffractograms were acquired in the angular range $2\theta$ between 5° and 50° in steps of 0.01°. The crystallinity and phase mixtures have been determined by Rietveld refinements to the XRD patterns.[36] The Rietveld refinement for $Pb_{1-x}Eu_x$–BDC ($x = 0.05, 0.10, 0.25, 0.50$) were performed with the GSAS/EXPGUI[37] software using as starting premise the atomic coordinates of the previously reported $[Pb(BDC)]_n$ (ref. 24–27) and $[Eu_2(BDC)_3(H_2O)_4]$[28,29] structures. The preferential orientation was corrected using the spherical harmonic model (tenth order) proposed by Jarvinen,[38] the peak profile was adjusted by the Thompson–Cox–Hastings function modified by Young and Desai (pV-TCHZ),[39,40] the surface roughness correction was refined by the Pitschke function and the background was fitted by an eighth-degree shifted Chebyshev polynomial function.[41] In the final run, the following parameters were refined: scale factor, background and absorption coefficients, spherical harmonic, unit-cell parameters and pV-TCHZ correction. The quantitative phase analysis was performed in accordance with the method proposed by Howard *et al.*[42]

### Single-crystal XRD of $Pb_{0.90}Eu_{0.10}$–BDC

Single crystals of the mixed-metal $Pb_{0.90}Eu_{0.10}$–BDC CPs were manually harvested from dried samples and immersed in highly viscous FOMBLIN Y perfluoropolyether vacuum oil (LVAC 140/13, Sigma-Aldrich).[43] Crystals were mounted on a Hampton Research CryoLoop with the help of a Stemi 2000 stereomicroscope equipped with Carl Zeiss lenses. XRD data were collected at 180(2) K on a Bruker X8 Kappa APEX II charge-coupled device (CCD) area-detector diffractometer (Mo $K_\alpha$ graphite-monochromated radiation, $\lambda = 0.7107$ Å) controlled by the APEX2 software package,[44] and an Oxford Instruments Cryostrem 700 Series low temperature device monitored remotely by the software interface Cryopad.[45] Diffraction images were processed using the software package SAINT+,[46] and data were corrected for absorption by the multiscan semi-empirical method implemented in SADABS.[47] The structure was solved using the algorithm implemented in SHELXT-2014,[48] which allowed the immediate location of almost all of the heaviest atoms composing the asymmetric unit. The remaining missing and misplaced non-hydrogen atoms were located from difference Fourier maps calculated from successive full-matrix least-squares refinement cycles on $F^2$ using the latest SHELXL from the 2014 release.[48,49] All structural refinements were performed using the graphical interface ShelXle.[50]

The inclusion of both $Pb^{2+}$ and $Eu^{3+}$ metallic centers in the crystal structure was achieved by restraining the atomic coordinates and the thermal parameters to common values. In later stages of the overall refinement, the site occupancies of the two metal centers were allowed to refine freely, ultimately converging to values close to 0.85 and 0.10, respectively. These values were fixed for the last refinement of the crystal structure, ultimately accounting for the inclusion of 5% of site vacancies and explaining the reason why the unit cell contains a non-integer number of atoms. Hydrogen atoms bound to carbon were placed at their idealized positions using the *HFIX 43* instruction in SHELXL. These hydrogen atoms were included in subsequent refinement cycles with isotropic thermal displacements parameters ($U_{iso}$) fixed at $1.2 \times U_{eq}$ of the parent carbon atoms.

Crystal data for $Pb_{0.90}Eu_{0.10}$–BDC: $C_8H_4Eu_{0.10}O_4Pb_{0.85}$, $M = 355.42$, orthorhombic, space group *Pbca*, $Z = 8$, $a = 7.6820(12)$ Å, $b = 10.2672(15)$ Å, $c = 18.256(3)$ Å, $V = 1439.9(4)$ Å$^3$, $\mu$(Mo-K$\alpha$) $= 20.768$ mm$^{-1}$, $D_c = 3.279$ g cm$^{-3}$, colorless prism with crystal size of $0.08 \times 0.06 \times 0.02$ mm$^3$. Of a total of 11 484 reflections collected, 1922 were independent ($R_{int} = 0.0452$). Final $R_1 = 0.0253[I > 2\sigma(I)]$ and w$R_2 = 0.0543$ (all data). Data completeness to theta = 25.24°, 99.8%. The last difference Fourier map synthesis showed the highest peak (1.476 e Å$^{-3}$) and the deepest hole (−1.406 e Å$^{-3}$) located at 0.69 and 0.78 Å from the mixed-metal site Pb1/Eu1, respectively. Structural drawings have been created using the software package Crystal Impact Diamond.[51]

Crystallographic data (including structure factors) for the crystal structure of compound $Pb_{0.90}Eu_{0.10}$–BDC have been deposited with the Cambridge Crystallographic Data Centre as supplementary publication no. CCDC 1490068.†

### Photoluminescence spectroscopy

Photoluminescence spectra were recorded on a Fluorolog-3® (Horiba scientific) with double-excitation spectrometer and a single-emission spectrometer (TRIAX 320) coupled to a R928 photomultiplier, using the front-face acquisition mode. The excitation source was a 450 W xenon lamp. The emission spectra were corrected for the spectral response of the excitation monochromator using a correction file provided by manufacture and the excitation spectra were weighed for the spectral distribution of the lamp intensity using a photodiode reference detector. Time-resolved emission spectra and emission decay curves were acquired using the same equipment with a pulsed Xe–Hg lamp ($6 \times 10^{-3}$ s pulse at half-width and $20–30 \times 10^{-6}$ s tail) as the excitation source. The emission quantum yields were measured using the C9920-02 from Hamamatsu system with a 150 W Xe lamp coupled to a monochromator for wavelength discrimination, an integration sphere as sample chamber and a multichannel analyzer for signal detection. Three measurements were made for each sample, and the average values obtained are reported with accuracy within 10% accorded to the manufacturer.

## Results and discussion

### XRD and PXRD studies

Fig. 1 shows the PXRD data collected for $[Pb(BDC)]_n$, $Pb_{1-x}Eu_x$–BDC, ($x = 0.05$, 0.10, 0.25, 0.50) and $[Eu_2(BDC)_3(H_2O)_4]$. The simulated patterns of the $[Pb(BDC)]_n$ and $[Eu_2(BDC)_3(H_2O)_4]$ compounds are also displayed. SEM images in Fig. 2 show that the size and morphology of the microcrystals are greatly influenced by the relative amount of incorporated $Eu^{3+}$ ions. Similarly to $[Pb(BDC)]_n$, the crystal habit of $Pb_{1-x}Eu_x$–BDC, with $x = 0.05$, 0.10, is based on block-like microcrystals. For $x = 0.10$, some crystals show the presence of a minor amount of smaller particles with a well-defined plate-like shape. These particles correspond to the $[Eu_2(BDC)_3(H_2O)_4]$ phase (see below). However, the $x = 10$ microcrystals chosen for single-crystal XRD studies do not shown evidence of any plate-like particles, as confirmed by the corresponding structural elucidation: a single phase mixed-metal $Pb_{0.90}Eu_{0.10}$–BDC CP (see below). In $Pb_{1-x}Eu_x$–BDC ($x = 0.25$ and 0.50) the block-like microcrystals are stacked together with well-defined platelets, analogous to those seen in $[Eu_2(BDC)_3(H_2O)_4]$, Fig. 2. This mixture of phases is also discerned in PXRD and photoluminescence data.

The PXRD patterns show clearly that the mixed-metal $Pb_{1-x}Eu_x$–BDC ($x = 0.05$ and 0.10) compounds are structurally similar to $[Pb(BDC)]_n$, whose structure was originally reported by Tan *et al.*[24] and later re-determined a handful of times.[25–27] This was unequivocally confirmed by Rietveld refinement, Fig. S1 and S2 (ESI†). Thus, we report the reader to these previous publications for additional structural details which are not described in this manuscript.

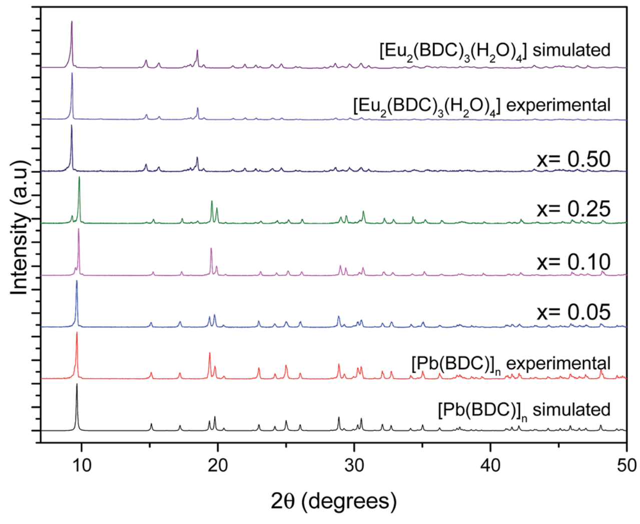

Fig. 1 Simulated patterns of $[Pb(BDC)]_n$ and $[Eu_2(BDC)_3(H_2O)_4]$ and PXRD patterns of $[Pb(BDC)]_n$, $Pb_{1-x}Eu_x$–BDC, with $x = 0.05$, 0.10, 0.25, 0.50, and $[Eu_2(BDC)_3(H_2O)_4]$.

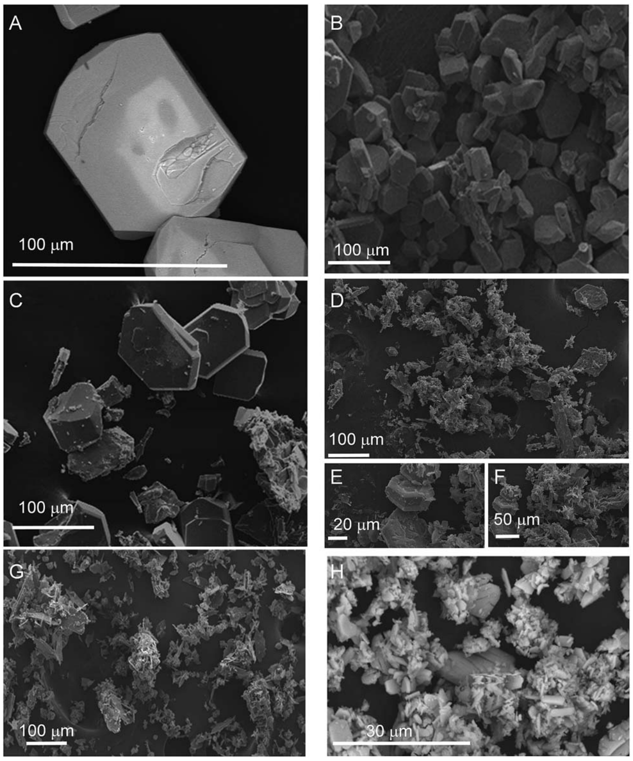

Fig. 2 SEM images of (A) $[Pb(BDC)]_n$, $Pb_{1-x}Eu_x$–BDC CPs (B) $x = 0.05$, (C) $x = 0.10$, (D–F) $x = 0.25$, (G) $x = 0.50$ and (H) $[Eu_2(BDC)_3(H_2O)_4]$.

For approximately an 0.25% inclusion of $Eu^{3+}$ a structural change occurs and $Pb_{0.75}Eu_{0.25}$–BDC is composed by a mixture of the $[Pb(BDC)]_n$ phase and another known CP structure solely based on $Eu^{3+}$:$[Eu_2(BDC)_3(H_2O)_4]$.[28,29] For this phase the $Eu^{3+}$ eight-coordination sphere involves six oxygen of the BDC ligand and two water molecules in a $C_4$ local pseudo-symmetry group.[29] Rietveld quantitative phase analysis reveals that $Pb_{0.75}Eu_{0.25}$–BDC has 0.90 and 0.10 of $[Pb(BDC)]_n$ and $[Eu_2(BDC)_3(H_2O)_4]$, respectively (Fig. S3, ESI†). These structures should be, somehow, related and to further investigate this we decided to employ a typical topological analysis in which each network is mathematically reduced into central nodes and connecting rods. Their selection needs, however, to be careful and structurally meaningful. Following the description by Alexandrov *et al.*,[52] who suggested that any moiety (ligand or atoms) connecting more than two metallic centers ($\mu_n$) should be considered as a network node, the center of gravity of the ligand itself was considered as a node, alongside with the metallic center. In this way, as revealed by the software package TOPOS, while $Pb_{0.90}Eu_{0.10}$–BDC is a 6,6-connected binodal network of the 6,6T23 topological type, $[Eu_2(BDC)_3(H_2O)_4]$ is instead a 4,4,6-connected trinodal framework belonging to the 4,4,6T24 family. We note that for both structures the metallic centers are 6-connected. Because of the smaller ionic radius of $Eu^{3+}$ and the absence of the lone pair of electrons of Pb$^{2+}$, in the latter framework the overall connectivity of the organic linkers is reduced from six to four.

$\mathrm{Pb}_{1-x}\mathrm{Eu}_x$–BDC, with $x = 0.50$ and 1.00, are structurally similar to $[\mathrm{Eu}_2(\mathrm{BDC})_3(\mathrm{H_2O})_4]$ (the Rietveld refinement for $x = 0.50$ is shown in Fig. S4, ESI†).

### Single-crystal XRD studies of $\mathrm{Pb}_{0.90}\mathrm{Eu}_{0.10}$–BDC

For approximately an 10% inclusion of Eu$^{3+}$ ($\mathrm{Pb}_{0.90}\mathrm{Eu}_{0.10}$–BDC), we were able to obtain single-crystals large enough which allowed an unequivocally structural elucidation using single-crystal XRD at low temperature. As expected, the unit cell parameters and space group match those previously reported for the pure Pb$^{2+}$ material,[24–27] showing that the three-dimensional network remain essentially unaltered. However, during the refinement stages, a charge problem arose: because of the inclusion of +3 charges at the sites of the +2 charges, and in the absence of voids capable of accommodate partially-occupied counter-ions to balance the crystal charge, the metallic center site has mandatorily to also be occupied by vacancies. Indeed, during the last stage of the refinement stage the site occupancies for Pb$^{2+}$ and Eu$^{3+}$ were allowed to refine freely, concerning to values of *ca.* 0.85 and 0.10, respectively. This agrees well with a presence of *ca.* 5% of vacancies while the crystal charge remains neutral.

The mixed-metal $\mathrm{Pb}_{0.90}\mathrm{Eu}_{0.10}$–BDC CP is based on a single metallic center (M), statistically occupied by *ca.* 85% of Pb$^{2+}$, 10% of Eu$^{3+}$ plus 5% of vacancies (Fig. 3).

As previously described for the other structural determinations,[24–27] the M center appear 7-coordinated, $\{\mathrm{MO_7}\}$, with the overall coordination polyhedron being significantly distorted due to the presence of a stereoactive lone pair of electrons belonging to the Pb$^{2+}$ metallic center. Indeed, considering the position of this lone pair of electrons as a possible coordination site, the overall coordination sphere resembles very much a highly distorted pentagonal bipyramid, with the M–O distances ranging between 2.483(4) and 2.775(4) Å. It is important to notice that there is a nearby oxygen atom from a carboxylate group which could be, in theory, interacting with the metallic center [at a distance of 3.037(4) Å]. A search in the Cambridge Structural Database (Version 5.37 with two updates – February 2016)[53] reveals that even though the known range of Pb–O interactions shows up distances up to 3.33 Å, the number of structures in which this appears is extremely small with the vast majority showing values around the mean value of 2.61 Å.

This coordination environment resembles a polyhedron with a $C_{2v}$ pseudo-symmetry. Taking into account the fact that when the Pb$^{2+}$ metallic center is replaced by Eu$^{3+}$ the lone pair is removed from the overall coordination polyhedron, it is thus feasible to assume that the Eu$^{3+}$ environment will readjust itself so to better accommodate the organic ligands. Ultimately, the Eu$^{3+}$ local symmetry is also changed, as we will discuss below.

The crystal packing of $\mathrm{Pb}_{0.90}\mathrm{Eu}_{0.10}$–BDC is rather featureless, being as depicted in Fig. 4 described as the parallel packing of inorganic metal oxide layers (in this compound with also *ca.* 5% of vacancies) placed in the *ab* plane of the unit cell, pillared along the [001] direction by the organic linkers. Though the structure is rich in oxygen atoms capable of accepting hydrogen atoms in supramolecular interactions, the structure only possesses such atoms attached to carbon which are also not located in a position to establish such interactions. Thus, no structurally-relevant supramolecular interactions exist in the present compound, being the packing

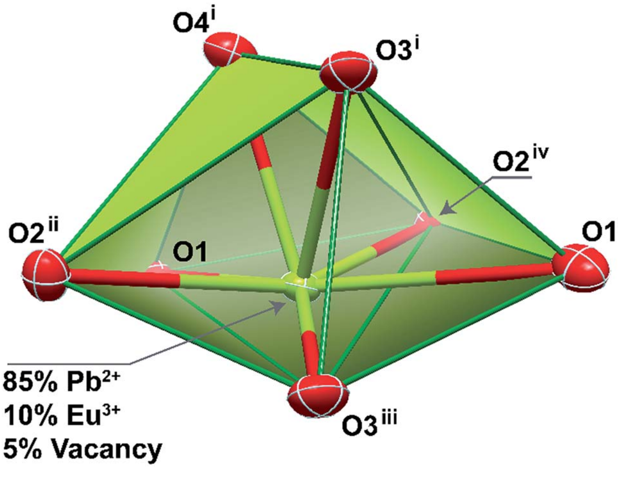

Fig. 3 Schematic representation of the highly distorted pentagonal bipyramidal coordination environment of the mixed-metal site present in compound $\mathrm{Pb}_{0.90}\mathrm{Eu}_{0.10}$–BDC. Atoms are represented as thermal ellipsoids drawn at the 80% probability level. Bond distances (in Å; M stands for Pb$^{2+}$ or Eu$^{3+}$): M1–O1 2.560(3); M1–O1$^{v}$ 2.775(4); M1–O2$^{ii}$ 2.623(3); M1–O2$^{iv}$ 2.652(3); M1–O3$^{i}$ 2.537(4); M1–O3$^{iii}$ 2.646(3); M1–O4$^{i}$ 2.483(4). Symmetry transformations used to generate equivalent atoms: (i) $x, -y + 3/2, z - 1/2$; (ii) $-x + 3/2, y + 1/2, z$; (iii) $-x + 2, y + 1/2, -z + 1/2$; (iv) $-x + 2, -y + 1, -z$; (v) $x + 1/2, -y + 3/2, -z$.

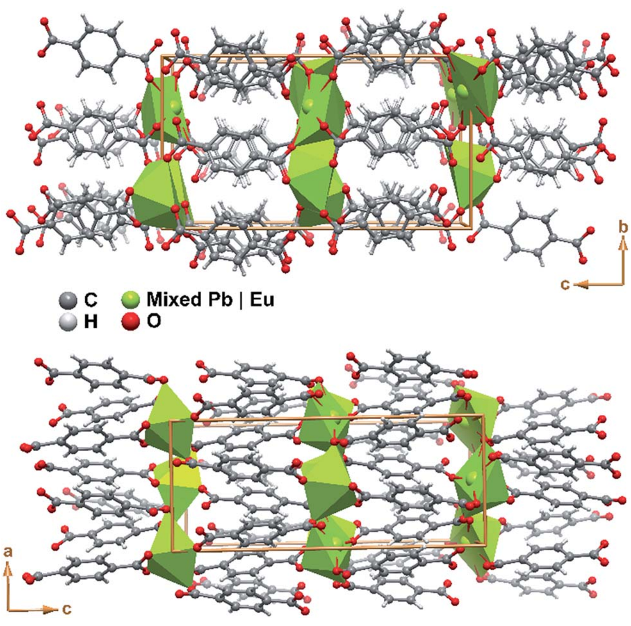

Fig. 4 Schematic representation of the crystal packing of compound $\mathrm{Pb}_{0.90}\mathrm{Eu}_{0.10}$–BDC viewed in perspective along the (top) [100] and (bottom) [010] directions of the unit cell.

solely driven by the coordination features to the metallic centers.

For higher concentration of $Eu^{3+}$ in the reactive gel (≥25%) the structure does not seem to be robust enough to accommodate the total inclusion of these optically-active metallic centers in the framework. This is most likely due to the fact that the amount of vacancies needed to maintain the crystal charge neutral is so large that the structure would collapse (or, in this case, it is not even formed).

## $Eu^{3+}$ luminescence as a structural local probe

Fig. 5 shows the emission spectra of the $Pb_{1-x}Eu_x$–BDC ($x$ = 0.05, 0.10, 0.25, 0.50) and $[Eu_2(BDC)_3(H_2O)_4]$ CPs. The relative intensity and number of Stark components of the $^5D_0 \rightarrow {}^7F_{0-4}$ transitions strongly depend on the $Eu^{3+}$ concentration, due to the presence of the $[Pb(BDC)]_n$ and $[Eu_2(BDC)_3(H_2O)_4]$ phases.

The emission spectra of $Pb_{1-x}Eu_x$–BDC ($x$ = 0.05, 0.10) display a single $^5D_0 \rightarrow {}^7F_0$ line (17 295.1 ± 3.0 $cm^{-1}$, 578.2 nm) and a local-field splitting of the $^7F_{1,2}$ levels in 3 and 6 components (at least), respectively. For $Pb_{0.5}Eu_{0.5}$–BDC, however, the $^5D_0 \rightarrow {}^7F_0$ transition red-shifts (17 268.2 ± 3.0 $cm^{-1}$, 579.1 nm) and the fewer number of $^7F_{1,2}$ Stark components detected (clearly 2 and 3, respectively) confirms the structural change from $[Pb(BDC)]_n$ to $[Eu_2(BDC)_3(H_2O)_4]$ pointed out by XRD. It is interesting to note that for $x = 0.25$ two $^5D_0 \rightarrow {}^7F_0$ lines are unequivocally observed, being characterized by the same energy values as those found for the lower and more concentrated CPs, indicating the presence of a phase mixture of $[Pb(BDC)]_n$ and $[Eu_2(BDC)_3(H_2O)_4]$, in accord with the PXRD data. To render easier the following discussion, the local environment of the $Eu^{3+}$ ions belonging to the $[Pb(BDC)]_n$ and $[Eu_2(BDC)_3(H_2O)_4]$ compounds will be hereafter termed as site 1 and site 2, respectively.

The number of $^7F_2$ Stark levels discerned for the $Pb_{1-x}Eu_x$–BDC ($x$ = 0.05 and 0.10) low-concentrated samples, 6 (arrows in Fig. 5A), is higher than the maximum $2J + 1$ allowed splitting, suggesting the presence of more than one $Eu^{3+}$ local environment. This is unequivocally confirmed by the dependence of the emission spectra of those compounds with the excitation wavelength, Fig. S5 (ESI†). In fact, for the $^5D_0 \rightarrow {}^7F_{1,2}$ transitions besides the Stark components ascribed to $Eu^{3+}$ ions in the $[Pb(BDC)]_n$ phase (site 1), it is possible to discern the presence of components from $[Eu_2(BDC)_3(H_2O)_4]$ (site 2), as highlighted by the vertical lines in Fig. 5A. The fact that the $[Eu_2(BDC)_3(H_2O)_4]$ structure is not detected by PXRD readily indicates that for the lower concentrated samples this phase appears in a very reduced relative amount, and thus the dominant local environment of the $Eu^{3+}$ ions belongs to the $[Pb(BDC)]_n$ phase (site 1). The emission spectra of $Pb_{0.5}Eu_{0.5}$–BDC are independent of the excitation wavelength, Fig. S5 (ESI†), indicating that the sample is formed only by the $[Eu_2(BDC)_3(H_2O)_4]$ phase.

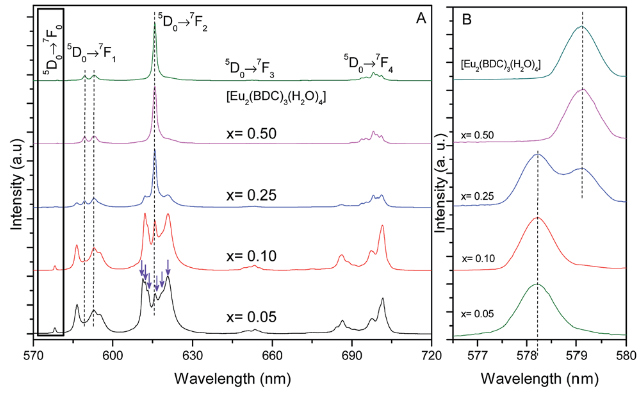

Fig. 5 (A) Emission spectra (300 K) of $Pb_{1-x}Eu_x$–BDC ($x$ = 0.05, 0.10, 0.25, 0.50) and $[Eu_2(BDC)_3(H_2O)_4]$ excited at 315 nm. (B) Magnification of the $^5D_0 \rightarrow {}^7F_0$ transition.

Whereas for site 2 each $Eu^{3+}$ ion occupies the center of a slightly distorted square plane, yielding a metal ion environment with pseudo-$C_4$ symmetry,[29] the discussion about the $Eu^{3+}$-local coordination in the $[Pb(BDC)]_n$ phase is, as far as we know, performed for the first time here. As mentioned above, the $Eu^{3+}$ ions in site 1 replace the structural position of the $Pb^{2+}$ ions in a $C_{2v}$ local symmetry group. When $Eu^{3+}$ replace $Pb^{2+}$ its local environment will readjust itself so to better accommodate the organic ligands and it is expectable a distortion from the $C_{2v}$ local symmetry group. Actually, the presence of the $^5D_0 \rightarrow {}^7F_0$ transition indicates a local point symmetry of the type $C_{nv}$ or $C_n$,[54,55] and the ligand field-splitting observed for the $^5D_0 \rightarrow {}^7F_{1,2}$ transitions are in agreement with this, even taken into account that the mentioned overlapping between the Stark components of the two phases for $Pb_{1-x}Eu_x$–BDC ($x$ = 0.05, 0.10 and 0.25). It is plausible that in this seven-fold first coordination sphere, the oxygen-ligating atom leading to a distorted $C_{2v}$ point symmetry contributes to decrease the rank 1 and 3 summations over spherical harmonics in the first coordination sphere (the main contributions to the $\Omega_2$ Judd–Ofelt intensity parameter), which would explain the noticeable decrease of the relative intensity of the $^5D_0 \rightarrow {}^7F_2$ transition, relatively to site 2 local symmetry.

Fig. 6 shows the excitation spectra of $Pb_{1-x}Eu_x$–BDC ($0.05 \leq x \leq 0.50$) and $[Eu_2(BDC)_3(H_2O)_4]$ monitored around the $Eu^{3+}$ $^5D_0 \rightarrow {}^7F_0$ transition revealing the presence of a broad band between 240 and 350 nm and a series of low-relative intensity intra-$4f^6$ transitions between the $F_0$ ground state and the $^5D_{4-1}$, $^5G_{2-6}$ and $^5L_6$ excited levels. The broad band is formed by one high-energy component centered at ~280 nm and by a low-energy one, whose peak position depends on the $Eu^{3+}$ amount, it peaks at ~312 nm for $0.05 \leq x \leq 0.25$ and at ~322 nm for $0.25 \leq x \leq 0.50$. A similar broad band with two components around 285 nm and 321 nm was also detected for the $Na_2BDC$, being ascribed to BDC excited states (Fig. S6, ESI†). Although the presence of ligand-to-metal charge transfer (LMCT) states which are expected in the range 300–350 nm cannot be ruled out,[56,57] we note that a similar broad band with two components around 285 nm and 321 nm was also detected for the $Na_2BDC$. Therefore, we assign the components in the excitation spectra to the preferential contribution of the BDC excited states (Fig. S6, ESI†), as we will detail below. The variation of the energy peak position with the $Eu^{3+}$ content can be ascribed to the dependence of the local coordination site on the $Eu^{3+}$ concentration, as it will be detailed below. Independently

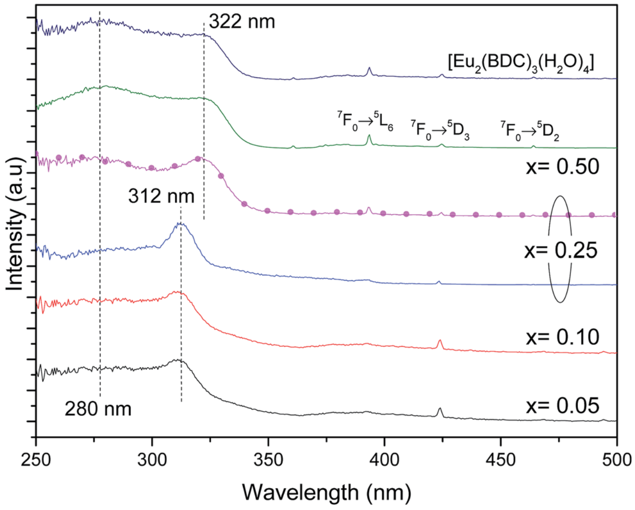

Fig. 6 Excitation spectra (300 K) of $Pb_{1-x}Eu_x$–BDC ($x = 0.05, 0.10, 0.25, 0.50$) and $[Eu_2(BDC)_3(H_2O)_4]$. The spectra were monitored at 578.2 nm for $x = 0.05$ and 0.10 and at 579.3 nm for $x = 0.50$ and $[Eu_2(BDC)_3(H_2O)_4]$. For $x = 0.25$ the excitation spectra were monitored at 578.2 nm (solid blue line) and at 579.1 nm (magenta line with circles).

of the $Eu^{3+}$ amount the higher relative intensity of the ligand-related components points out that the $Eu^{3+}$ excited states are mainly sensitized by the ligands rather than by direct intra-$4f^6$ excitation.

We note that for $x = 0.25$, the excitation spectra depend on the monitoring wavelength being observed a red-shift of the low-energy component from 312 nm to 322 nm, as the monitoring wavelength increases from 578.2 nm (site 1) to 579.1 nm (site 2), readily indicating that the $Eu^{3+}$ excited states in each local coordination are distinctly populated. Thus, the $Pb_{0.75}Eu_{0.25}$–BDC CP can be used to demonstrate the $Eu^{3+}$ ability as a spectroscopic local probe. As above described, there are unequivocal experimental evidences supporting the presence of site 1 and site 2 at $x = 0.25$ with energy values for the $^5D_0 \rightarrow {}^7F_0$ transition of 17 268.2 ± 3.0 $cm^{-1}$ (579.1 nm) and 17 295.1 ± 3.0 $cm^{-1}$ (578.2 nm), respectively. Usually, site-selective excitation in $Eu^{3+}$ compounds was performed using a tunable dye laser.[55,58,59] The $Pb_{0.75}Eu_{0.25}$–BDC CP is one of the rare examples in which two $Eu^{3+}$ sites can be selectively excited through a common Xe lamp, as evidenced below.

The high-resolution excitation spectra were monitored at the $^5D_0 \rightarrow {}^7F_0$ energy values of site 1 and site 2 for $Pb_{0.75}Eu_{0.25}$–BDC CP, Fig. 7. The spectra show the BDC ligand-related bands at ~288 nm and ~312 nm for site 1, being observed an enlargement and a shift of these components to ~275 nm and ~322 nm, respectively, when site 2 is monitored.

While monitoring site 1, the component at 366 nm shows an increase in its relative intensity, indicating that the $Eu^{3+}$ ions at site 1 are preferentially excited at this wavelength. We note that while monitoring site 2, it is observed a significant enhancement of the relative intensity of the higher-energetic component, thus, indicating that under excitation around 288 nm, site 2 is favored with respect to the emission arising from site 1. Moreover, site 2 is also favored under direct-intra-$4f^6$ excitation, as the higher relative intensity of the $Eu^{3+}$ transitions (in comparison with that in the excitation spectrum monitored within site 1) points out.

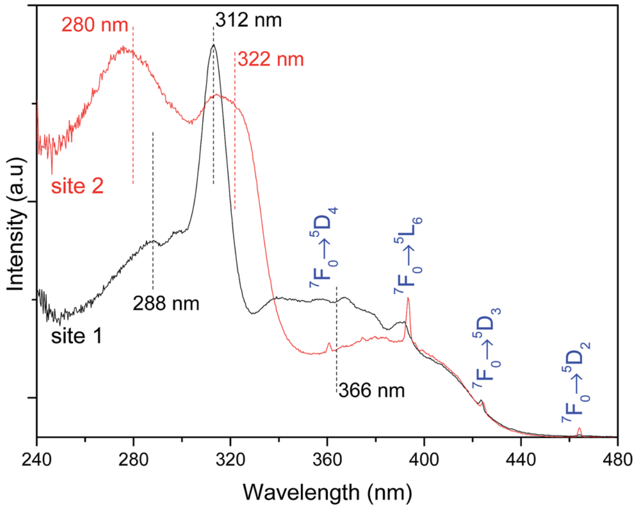

Fig. 7 Excitation spectra (300 K) of $Pb_{0.75}Eu_{0.25}$–BDC CP monitored within the $^5D_0 \rightarrow {}^7F_0$ transitions at 578.2 nm (site 1, black line) and 579.3 nm (site 2, red line). The vertical lines assign the BDC ligand-related components.

Based on the information provided by the selective monitoring of the excitation paths that preferentially populate the $^5D_0$ excited states of the $Eu^{3+}$ at site 1 and site 2, Fig. 8 shows the emission spectra dependence on the excitation wavelength for $Pb_{0.75}Eu_{0.25}$–BDC. Fig. 8 shows that while exciting site 2 at 366 nm the emission spectrum resembles that of $[Eu_2(BDC)_3(H_2O)_4]$, whereas at 280 nm, the spectrum drastically changes being similar to that of the $Pb_{0.95}Eu_{0.05}$–BDC CP.

The $^5D_0$ lifetime values were determined by selectively monitoring the emission at the $^5D_0 \rightarrow {}^7F_0$ transitions at 578.0 nm (site 1) and 579.0 nm (site 2) and under the same

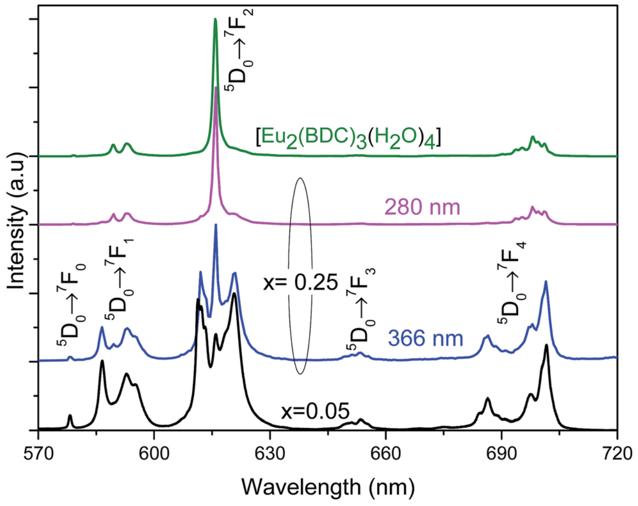

Fig. 8 Emission spectra (300 K) of $Pb_{1-x}Eu_x$–BDC excited at 280 mm and at 366 nm for $x = 0.25$ and excited at 315 nm for $x = 0.05$ and $[Eu_2(BDC)_3(H_2O)_4]$.

Table 1 $^5D_0$ lifetime values at 300 K (ms) for $Pb_{1-x}Eu_x$–BDC ($x$ = 0.05, 0.10, 0.25, 0.50) (site 1 and site 2)

| $x$ | Site 1 | Site 2 |
|---|---|---|
| 0.05 | 1.21 ± 0.07 | |
| 0.10 | 1.00 ± 0.10 | |
| 0.25 | 0.90 ± 0.03 | 0.40 ± 0.01 |
| 0.50 | | 0.42 ± 0.01 |
| 1.00 | | 0.44 ± 0.01 |

excitation wavelength (315 nm). All the emission decay curves are well reproduced by a single-exponential function (Fig. S7–S12, ESI†), yielding the lifetime values listed in Table 1. The $^5D_0$ lifetime values are higher for site 1 compared with that found for site 2, which can be ascribed to the presence of water molecules coordinated to the $Eu^{3+}$ placed in site 2, which favors the non-radiative transition probability through OH oscillators. We also note that the increase of $Eu^{3+}$ concentration causes a decrease in the $^5D_0$ lifetime values of site 1, suggesting the presence of concentration quenching effects. For site 2, the $^5D_0$ lifetime values are almost independent of the $Eu^{3+}$ concentration.

The distinct $^5D_0$ lifetime values of site 1 and site 2 were rationalized in terms of the calculation of the $^5D_0$ radiative ($A_r$) and nonradiative ($A_{nr}$) transition probabilities and of the $^5D_0$ quantum efficiency ($\eta$) following a methodology described elsewhere.[60] These calculations were performed for $Pb_{0.95}Eu_{0.05}$–BDC, site 1, and for $[Eu_2(BDC)_3(H_2O)_4]$, site 2. We note that the very close $\eta$ values (0.27 and 0.21, respectively), result from distinct contributions from $A_r$ and $A_{nr}$. Despite higher $A_r$ values (0.479 $ms^{-1}$) found for $[Eu_2(BDC)_3(H_2O)_4]$ compared with that (0.224 $ms^{-1}$) of $Pb_{0.95}Eu_{0.05}$–BDC, we note the increase of $A_{nr}$ for site 2 ($[Eu_2(BDC)_3(H_2O)_4]$, 1.794 $ms^{-1}$) relatively to that in site 1 ($Pb_{0.95}Eu_{0.05}$–BDC, 0.602 $ms^{-1}$). The higher value of the $A_{nr}$ value for the $[Eu_2(BDC)_3(H_2O)_4]$ can be ascribed to the presence of 4 water molecules in the coordination sphere which are known as very efficient quenchers from the $^5D_0$ emission.[60]

The different $^5D_0$ lifetime values of site 1 and site 2 allow the use of time-resolved spectroscopy to distinguish the Stark components that arise from each site, as illustrated for the most intense $^5D_0 \rightarrow {}^7F_2$ transition. Fig. 9 shows the time-resolved emission excited at 315 nm acquired under distinct starting-delay (SD) values in the spectral regions of the $^5D_0 \rightarrow {}^7F_{0,2}$ transitions. At shorter SD values (0.05 ms), the emission spectrum reveals two lines for the $^5D_0 \rightarrow {}^7F_0$ transition region (already detected under steady-state mode, Fig. 5) ascribed to site 1 (578 nm) and site 2 (579 nm). At longer SD values (2.50 ms), only the long-lived $^5D_0 \rightarrow {}^7F_0$ transition from site 1 remains, corroborating the longer $^5D_0$ lifetime values listed in Table 1. At shorter SD values (0.05 ms) the $^5D_0 \rightarrow {}^7F_2$ spectral region is dominated by the short-lived line at 616 nm ascribed to site 2, whereas for longer SD values (2.50 ms) the emission is governed by the long-lived Stark components at 612.0 nm (16 340 ± 3 $cm^{-1}$) and 621.0 nm (16 103 ± 3 $cm^{-1}$) characteristic of site 1, Fig. 5B.

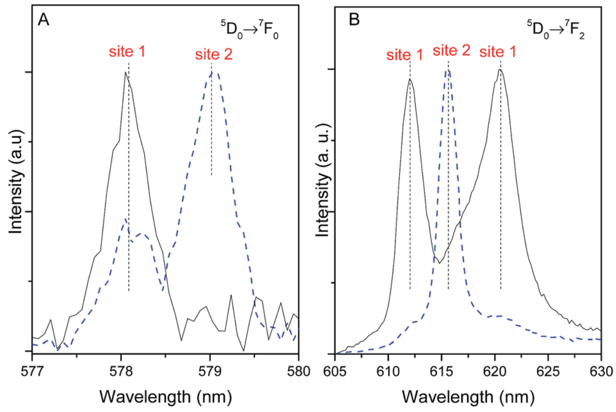

Fig. 9 Time-resolved emission spectra of $Pb_{0.75}Eu_{0.25}$–BDC (300 K) in the (A) $^5D_0 \rightarrow {}^7F_0$ and (B) $^5D_0 \rightarrow {}^7F_2$ spectral regions, excited at 315 nm and acquired at SD = 0.05 ms (dashed line) and SD = 2.50 ms (solid line) with an integration window of 0.05 and 20 ms, respectively.

The emission properties of the CPs were further quantified by measuring the emission quantum yield as a function of the excitation wavelength, namely through the ligands excited states (280–370 nm) and *via* direct intra-$4f^6$ excitation ($^5L_6$, 393 nm and $^5D_2$, 465 nm), Fig. 10. The higher emission quantum yield was found for the $Pb_{0.75}Eu_{0.25}$–BDC, 69 ± 7%, under excitation at 315 nm, which is well above the values found for similar materials based on Pb(II).[21,23] Analyzing the dependence of the emission quantum yield on the $Eu^{3+}$ amount it is observed that the maximum values (independent of the excitation wavelengths) are found for $x = 0.25$ which may be ascribed to the simultaneous contribution of site 1 and site 2 for the radiative emission. Focusing our attention into the low-concentrated samples (site 1), it is observed that under the ligands-preferential excitation at 315 nm (Fig. 6), the emission quantum yield increases as $x$ increases from 0.05 to 0.25 which may be attributed to the fact that as the amount of $Eu^{3+}$ increases there is a larger number of ligands with $Eu^{3+}$ ions in the neighborhoods, thus, the ligand-to-$Eu^{3+}$ energy transfer is

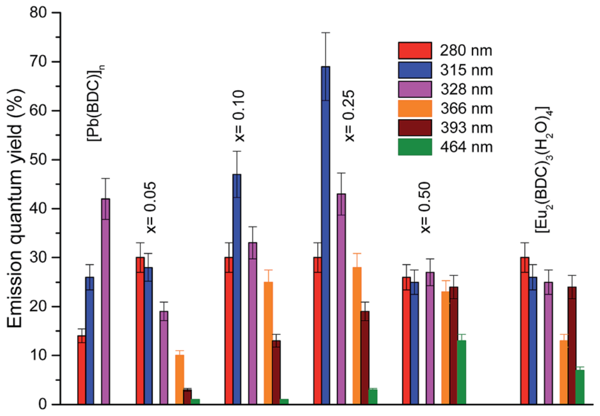

Fig. 10 Dependence of the emission quantum yield on the excitation wavelengths for $[Pb(BDC)]_n$, $Pb_{1-x}Eu_x$–BDC ($x$ = 0.05, 0.10, 0.25, 0.50) and $[Eu_2(BDC)_3(H_2O)_4]$.

favored. Another interesting aspect is that when the intra-4f$^6$ levels are excited (393 nm, 465 nm), the quantum yield is larger for the more concentrated samples, $Pb_{1-x}Eu_x$–BDC, $x = 0.25$, 0.50 and $[Eu_2(BDC)_3(H_2O)_4]$, in good agreement with the preferential excitation of site 2 under direct intra-4f$^6$ excitation.

The quantum yield values for $Pb_{0.95}Eu_{0.05}(BDC)$ and $[Eu_2(BDC)_3(H_2O)_4]$ are analogous the values found for the $^5D_0$ quantum efficiency. It is known that the quantum efficiency $\eta$ is the superior limit for $q$ ($q \leq \eta$)[60] and that the overall absolute emission quantum yield $q$ is the product of the sensitization efficiency of the ligand ($\eta_{tr}$) and $\eta$, $q = \eta_{tr} \times \eta$.[61] The similarity between $q$ and $\eta$ points out that an efficient ligand-to-Eu$^{3+}$ energy transfer ($\eta_{tr} \sim 1$) occurs for those CPs. This conclusion is in good agreement with the absence of LMCT bands in the excitation spectra (Fig. 6) which are known to play an important role in quenching the Eu$^{3+}$ luminescence.[57]

## Conclusions

We provide an intriguing example of a series of luminescent mixed-metal $Pb_{1-x}Eu_x$–BDC ($x = 0.05, 0.10, 0.25, 0.50$) CPs, including, for comparison purposes, the mononuclear $[Pb(BDC)]_n$ and $[Eu_2(BDC)_3(H_2O)_4]$ phases. Increasing the amount of Eu$^{3+}$, the mixed-metal CPs display a gradual change in their structure from the $[Pb(BDC)]_n$ phase to the $[Eu_2(BDC)_3(H_2O)_4]$ one, well-monitored through luminescence spectroscopy. In fact, the discussion about the Eu$^{3+}$-local coordination in the $[Pb(BDC)]_n$ phase is, as far as we know, performed for the first time here. The $Pb_{0.75}Eu_{0.25}$–BDC material display a mixture of both crystalline phases with a high emission quantum yield of 69 ± 7%, one the highest value measured for luminescent CPs based on Pb(II). Moreover, the $Pb_{0.75}Eu_{0.25}$–BDC CP is one of the rare examples in which two Eu$^{3+}$ sites can be selectively excited through a common Xe lamp illustrating how powerful the Eu$^{3+}$ luminescence is as a local probe spectroscopic tool.

## Acknowledgements

The authors gratefully acknowledge CNPq (RH-INCT/INAMI), DPP-UNB, FAP-DF, and CAPES for financial support. This work was partially developed in the scope of the project CICECO – Aveiro Institute of Materials (Ref. FCT UID/CTM/50011/2013), financed by Portuguese funds through the FCT/MEC and when applicable co-financed by FEDER under the PT2020 Partnership Agreement. LDC acknowledges CAPES and CNPq (Brazil) for a Pesquisador Visitante Especial grant (313778/2013-2) within the Science without Borders program.

## References

1 J. Heine and K. Muller-Buschbaum, *Chem. Soc. Rev.*, 2013, **42**, 9232–9242.
2 H. Furukawa, K. E. Cordova, M. O'Keeffe and O. M. Yaghi, *Science*, 2013, **341**, 1230444.
3 T. Wen, D.-X. Zhang, J. Liu, R. Lin and J. Zhang, *Chem. Commun.*, 2013, **49**, 5660–5662.
4 G. Férey, *New J. Chem.*, 2016, **40**, 3950–3967.
5 M. D. Allendorf, C. A. Bauer, R. K. Bhakta and R. J. T. Houk, *Chem. Soc. Rev.*, 2009, **38**, 1330–1352.
6 J. Rocha, L. D. Carlos, F. A. A. Paz and D. Ananias, *Chem. Soc. Rev.*, 2011, **40**, 926–940.
7 B. Zhao, X.-Y. Chen, P. Cheng, D.-Z. Liao, S.-P. Yan and Z.-H. Jiang, *J. Am. Chem. Soc.*, 2004, **126**, 15394–15395.
8 T. R. Cook, Y.-R. Zheng and P. J. Stang, *Chem. Rev.*, 2012, **113**, 734–777.
9 H. Deng, C. J. Doonan, H. Furukawa, R. B. Ferreira, J. Towne, C. B. Knobler, B. Wang and O. M. Yaghi, *Science*, 2010, **327**, 846–850.
10 A. D. Burrows, *CrystEngComm*, 2011, **13**, 3623–3642.
11 G. Férey, F. Millange, M. Morcrette, C. Serre, M. L. Doublet, J. M. Grenèche and J. M. Tarascon, *Angew. Chem., Int. Ed. Engl.*, 2007, **46**, 3259–3263.
12 H.-L. Gao, B. Zhao, X.-Q. Zhao, Y. Song, P. Cheng, D.-Z. Liao and S.-P. Yan, *Inorg. Chem.*, 2008, **47**, 11057–11061.
13 W. Kleist, M. Maciejewski and A. Baiker, *Thermochim. Acta*, 2010, **499**, 71–78.
14 V. Singh, A. Kumar, M. K. Yadav, L. B. Prasad and N. Singh, *Synth. Met.*, 2013, **176**, 65–69.
15 F. Gul-E-Noor, M. Mendt, D. Michel, A. Pöppl, H. Krautscheid, J. Haase and M. Bertmer, *J. Phys. Chem. C*, 2013, **117**, 7703–7712.
16 Y.-H. Zhao, H.-B. Xu, K.-Z. Shao, Y. Xing, Z.-M. Su and J.-F. Ma, *Cryst. Growth Des.*, 2007, **7**, 513–520.
17 J. He, M. Zeller, A. D. Hunter and Z. Xu, *J. Am. Chem. Soc.*, 2011, **134**, 1553–1559.
18 J. Chen, Q. Zhang, Z.-F. Liu, S.-H. Wang, Y. Xiao, R. Li, J.-G. Xu, Y.-P. Zhao, F.-K. Zheng and G.-C. Guo, *Dalton Trans.*, 2015, **44**, 10089–10096.
19 L.-Q. Fan, L.-M. Wu and L. Chen, *Inorg. Chem.*, 2006, **45**, 3149–3151.
20 J.-D. Lin, S.-T. Wu, Z.-H. Li and S.-W. Du, *CrystEngComm*, 2010, **12**, 4252–4262.
21 W. W. Lestari, P. Lönnecke, H. C. Streit, M. Handke, C. Wickleder and E. Hey-Hawkins, *Eur. J. Inorg. Chem.*, 2014, 1775–1782.
22 Y. Wang, Z. J. Zhang, W. Shi, P. Cheng, D. Z. Liao and S. P. Yan, *CrystEngComm*, 2010, **12**, 1086–1089.
23 M. Pan, C. Yan, L. Chen, L. Y. Zhang, S. Y. Yin, Y. X. Zhu, K. Wu, Y. J. Hou and C. Y. Su, *New J. Chem.*, 2015, **39**, 3770–3776.
24 Y.-X. Tan, F.-Y. Meng, M.-C. Wu and M.-H. Zeng, *J. Mol. Struct.*, 2009, **928**, 176–181.
25 K.-F. Wu, F. Jiang, X.-L. Bai, S.-Y. Mo, G.-F. Qin and Y. Feng, *J. Inorg. Organomet. Polym. Mater.*, 2015, **25**, 879–885.
26 L. Zhang, Z.-J. Li, Q.-P. Lin, Y.-Y. Qin, J. Zhang, P.-X. Yin, J.-K. Cheng and Y.-G. Yao, *Inorg. Chem.*, 2009, **48**, 6517–6525.
27 Z.-P. Li, Y.-H. Xing, C.-G. Wang, J. Li, X.-Q. Zeng, M.-F. Ge and S.-Y. Niu, *Z. Anorg. Allg. Chem.*, 2009, **635**, 1650–1653.
28 T. M. Reineke, M. Eddaoudi, M. Fehr, D. Kelley and O. M. Yaghi, *J. Am. Chem. Soc.*, 1999, **121**, 1651–1657.
29 C. Daiguebonne, N. Kerbellec, O. Guillou, J.-C. Bünzli, F. Gumy, L. Catala, T. Mallah, N. Audebrand, Y. Gérault, K. Bernot and G. Calvez, *Inorg. Chem.*, 2008, **47**, 3700–3708.

30 J. W. Stouwdam, G. A. Hebbink, J. Huskens and F. C. J. M. van Veggel, *Chem. Mater.*, 2003, **15**, 4604–4616.

31 G. T. Xiang, J. H. Zhang, Z. D. Hao, X. Zhang, G. H. Pan, Y. S. Luo and H. F. Zhao, *CrystEngComm*, 2015, **17**, 3103–3109.

32 K. Devlin, B. Okelly, Z. R. Tang, C. Mcdonagh and J. F. Mcgilp, *J. Non-Cryst. Solids*, 1991, **135**, 8–14.

33 S. J. L. Ribeiro, K. Dahmouche, C. A. Ribeiro, C. V. Santilli and S. H. Pulcinelli, *J. Sol–Gel Sci. Technol.*, 1998, **13**, 427–432.

34 D. Q. Chen, Y. Zhou, Z. Y. Wan, H. Yu, H. W. Lu, Z. G. Ji and P. Huang, *Phys. Chem. Chem. Phys.*, 2015, **17**, 7100–7103.

35 S. Y. Qi, Y. L. Huang, Y. D. Li, P. Cai, S. I. Kim and H. J. Seo, *J. Mater. Chem. B*, 2014, **2**, 6387–6396.

36 H. M. Rietveld, *J. Appl. Crystallogr.*, 1969, **2**, 65–71.

37 A. C. Larson and R. B. Von Dreele, *General Structure Analysis System (GSAS)*, Los Alamos National Laboratory, 2004.

38 M. Jarvinen, *J. Appl. Crystallogr.*, 1993, **26**, 525–531.

39 P. Thompson, D. E. Cox and J. B. Hastings, *J. Appl. Crystallogr.*, 1987, **20**, 79–83.

40 R. Young and P. Desai, *Arch. Nauki Mater.*, 1989, **10**, 71–90.

41 V. Sidey, *J. Appl. Crystallogr.*, 2004, **37**, 1013–1014.

42 R. Hill and C. Howard, *J. Appl. Crystallogr.*, 1987, **20**, 467–474.

43 T. Kottke and D. Stalke, *J. Appl. Crystallogr.*, 1993, **26**, 615–619.

44 *APEX2, Data Collection Software Version 2.1-RC13*, Bruker AXS, Delft, The Netherlands, 2006.

45 *Cryopad, Remote monitoring and control, Version 1.451*, Oxford Cryosystems, Oxford, United Kingdom, 2006.

46 *SAINT+, Data Integration Engine v. 8.27b©*, Bruker AXS, Madison, Wisconsin, USA, 1997-2012.

47 G. M. Sheldrick, *SADABS 2012/1, Bruker AXS Area Detector Scaling and Absorption Correction*, Bruker AXS, Madison, Wisconsin, USA, 2012.

48 G. M. Sheldrick, *SHELXT-2014, Program for Crystal Structure Solution*, University of Göttingen, 2014.

49 G. M. Sheldrick, *Acta Crystallogr., Sect. A: Found. Crystallogr.*, 2008, **64**, 112–122.

50 C. B. Hübschle, G. M. Sheldrick and B. Dittrich, *J. Appl. Crystallogr.*, 2011, **44**, 1281–1284.

51 K. Brandenburg, *DIAMOND, Version 3.2f*, Crystal Impact GbR, Bonn, Germany, 1997-2010.

52 E. Alexandrov, V. Blatov, A. Kochetkov and D. Proserpio, *CrystEngComm*, 2011, **13**, 3947–3958.

53 C. R. Groom, I. J. Bruno, M. P. Lightfoot and S. C. Ward, *Acta Crystallogr., Sect. B: Struct. Sci., Cryst. Eng. Mater.*, 2016, **72**, 171–179.

54 L. D. Carlos and A. L. L. Videira, *Phys. Rev. B*, 1994, **49**, 11721–11728.

55 K. Binnemans, *Coord. Chem. Rev.*, 2015, **295**, 1–45.

56 Y. Hasegawa and T. Nakanishi, *RSC Adv.*, 2015, **5**, 338–353.

57 S. V. Eliseeva, O. V. Kotova, F. Gumy, S. N. Semenov, V. G. Kessler, L. S. Lepnev, J. C. G. Bunzli and N. P. Kuzmina, *J. Phys. Chem. A*, 2008, **112**, 3614–3626.

58 J. C. G. Bunzli and G. O. Pradervand, *J. Chem. Phys.*, 1986, **85**, 2489–2497.

59 M. M. Fernandes, M. Schmidt, T. Stumpf, C. Walther, D. Bosbach, R. Klenze and T. Fanghanel, *J. Colloid Interface Sci.*, 2008, **321**, 323–331.

60 L. D. Carlos, R. A. S. Ferreira, V. de Zea Bermudez and S. J. L. Ribeiro, *Adv. Mater.*, 2009, **21**, 509–534.

61 J.-C. G. Bünzli, *Chem. Rev.*, 2010, **110**, 2729–2755.